Experimental Analysis of Heat Transfer and Multi Objective Optimization of Swirling Jet Impingement on a Flat Surface

S. Mohamed Illyas[1†], B. R. Ramesh Bapu[2] and V. Venkata Subba Rao[1]

[1] Department of Mechanical Engineering, Jawaharlal Nehru Technological University, Kakinada-533003, India
[2] Department of Mechanical Engineering, Chennai Institute of Technology, Chennai-600069, India

†*Corresponding Author Email: illyas1978@gmail.com*

ABSTRACT

The influence of swirling flow on distribution of wall heat transfer on a flat plate with helicoid swirl inserts is experimentally studied. The focus of the study is on the swirling effect imposed by helicoid surfaces. Six helicoid swirl inserts of single vane, double vanes and triple vanes with swirl number (*Sw*) of 0.75 and 1.1 are used in this study. The heat transfer measurements are made for the Reynolds number range of 12700 - 32700 and for the nozzle exit to impinging plate distance (H/D) of 1, 2, 3 and 4 using thermo chromic liquid crystal technique. The swirling impinging jet is also compared with circular impinging jet on the heat transfer performance. The obtained experimental results provide the information on the behavior of single, double and triple helicoid swirl inserts on the heat transfer performance. The experimental values are analyzed with multi objective optimization technique of principle component analysis by computing multi response performance index (MRPI). Their performance is presented in terms of heat transfer rate through evaluation of Nusselt number on the impinging surface and heat transfer uniformity and decay of Nusselt number. The principle component analysis reveals that the double helicoid with higher *H/D* ratio improves performance of the swirling jet with relatively higher computed MRPI. It is found from the analysis of variance (ANOVA) that the *H/D* ratio contributes significant effect on the output followed by number of helicoid vanes and swirl number.

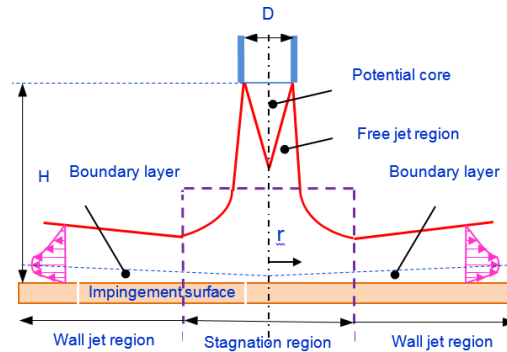Keywords*: Heat transfer; Swirling impinging jet; Thermochromic liquid crystal; Optimization.*

NOMENCLATURE

A	surface area of stainless steel sheet	q_{in}	heat input
D	outside diameter of helicoid vane	q_{cond}	conduction heat loss
d	diameter of helicoid vane hub	$q_{free\,conv}$	free convection heat loss
H/D	distance between the nozzle exit and the impinging surface, dimensionless	q_{rad}	radiation heat loss
		$t_w(r)$	average temperature along circumferential direction on the impinging surface at radius r
h	convective heat transfer coefficient		
k_{steel}	thermal conductivity of stainless steel sheet		
		T_j	temperature of jet at pipe exit
k_{TLC}	thermal conductivity of TLC sheet	T_a	ambient temperature
Nu	Nusselt number		
Nu_{avg}	average Nusselt Number Distribution	u	air velocity in the smooth pipe
Nu_{decay}	Nusselt number decay		
Re	Reynolds number	γ_a	kinematic viscosity of air
r/D	radial distance measured on the impinging plate, Dimensionless	σ	stefan boltzmann constant
		ϵ_{TLC}	emissivity of TLC sheet
Sw	Swirl number	ξ	non uniformity index
t_{steel}	thickness of stainless steel sheet	ϕ	angle of helicoid vane, degrees
t_{TLC}	thickness of TLC sheet	Δ	uncertainty

1. INTRODUCTION

Impinging jets are being used for heat transfer enhancement in the engineering applications such as cooling of hot steel plates, electronic components, turbine blades, glass tempering and drying of food products and papers. The flow characteristics of circular impinging jet (Dae *et al.*, 2004) depends on the diameter of the nozzle and nozzle to impinging surface distance can be categorized according to Viskanta (1993) as free jet region, impingement region (stagnation region) and wall jet region as shown in Fig.1. In the free jet region, the emerging jet creates shearing at the edges due to velocity gradient that produces outward momentum laterally, raising the mass flow of the jet. The free jet region consists of a potential core zone (Viskanta, 1993) where its velocity remains constant and is equal to exit jet velocity. The potential core length depends on the intensity of turbulence at flow exit and initial velocity profile. The stagnation region is characterized by the impingement zone where the jet builds up a higher static pressure on the impingement surface and turns radially. In the wall jet region, the jet spreads in radial direction and its velocity decreases with increasing radial distance from stagnation region. In the case of circular impinging jet, high heat transfer rates are associated in the stagnation region due to thin boundary layer and rapid decay of heat transfer in wall jet region caused by the further development of boundary layer which produces non uniform heat transfer on the impinging surface. In some applications like cooling of electronic components, a higher rate of heat transfer with radial uniformity is required.

Heat transfer and flow characteristics of impinging jet have been studied by many authors. Huang *et al.* (1998) studied the heat transfer and flow characteristics of circular and swirling impinging jets for nozzle to plate distances of 12.7 mm, 25.4 mm, 50.8 mm and 76.2 mm. They used cylindrical insert with four narrow grooves as a swirl device (swirl angle $\theta = 15°$, $30°$ and $45°$) and reported that radial distribution of Nusselt number is more uniform for swirling flow than for non swirling flow at higher swirl angle and larger nozzle to plate distances. Wae-Hayee *et al.* (2015) studied heat transfer and flow characteristics of in line round impinging jet with the cross flow effect of fixed jet velocity ($Re = 13400$) and varying cross flow velocity (jet velocity/cross flow velocity, VR = 3,5 and 7). They reported that the interaction of impinging jet and cross jet enhances stagnation Nusselt number and it is highest at VR = 3 with reduction in average Nusselt number distribution. Yuan *et al.* (2006) experimentally studied CO_2 jet impingement for the Reynolds number range of 7500 - 28300 and reported that the swirling flow significantly improves radial uniformity on the impinging surface. Their study is limited to fixed swirling angle and nozzle to plate distance. Dae *et al. et al.* (2002) examined the Nusselt number variation on a heated surface with swirling impinging jet using vane type swirl generator with swirl number varying from 0 to 0.77 and found better uniformity in heat transfer at higher swirl number $Sw = 0.77$ reporting that the swirling effect is insignificant at larger nozzle to plate distance ($H/D = 10$).

Fig.1. Flow structure of circular impinging jet.

Fenot *et al.* (2015) conducted heat transfer studies on multi-channel impinging jet by comparing heat transfer distribution from a hot jet issued from a circular nozzle and a swirling nozzle with $Sw = 0$ and 0.26. They reported that the Nusselt number increases for the swirling impinging jet at lower separation distance ($H/D =1$) and it decreases with increasing separation distance ($H/D = 6$) compared with circular jet. Bakirci and Bilen (2007) evaluated heat transfer rate on the impinging surface using swirl insert having four narrow slots on its surface with swirl angles 0°, 22.5°, 41° and 50° reporting that the location of heat transfer peaks radially moves away from the stagnation point with increasing swirl angle. They concluded that lower Reynolds number (10,000) and higher nozzle to surface distance ($H/D = 14$) exhibit more uniform Nusselt number distribution with reduction in its magnitude. Luai M. Al-Hadhrami (2010) investigated the heat transfer characteristics of staggered impinging jet on inclined target surface for three different exit flow cases (coincident and opposed with the entry flow and combined: cases 1 2 and 3 respectively) with Reynolds number Re = 9400,14400,18800 and feed channel aspect ratio of 5,7 and 9. He reported that due to smaller cross flow effects case 1 and case 3 exhibit higher average Nusselt number distribution compared with case 2 and the influence of feed channel aspect ratio is marginal on the heat transfer rate on the impinging surface. Andrea Cardone (2012) studied heat transfer distribution on a flat surface using helical inserts of swirl number $Sw = 0$, 0.2, 0.4, 0.6 and 0.8 and reported that at fixed H/D distance, increasing the swirl number broadens the impingement region and decreases the heat transfer rate. Yang *et al.* (2010) examined the wall pressure, flow and heat transfer characteristics of round and swirling jets. They conducted experiments with fixed Reynolds and swirl numbers ($Re = 7000$, Sw = 0.92) at varying separation distances ($H/D = 0.3$-8.1) reporting that at short and intermediate H/D distances the reverse flow streams are evident and at the increasing H/D distance the reverse flow streams combine to form a single stream. Koichi *et al.* (2010) presented the heat transfer characteristics of swirling impinging jet in laminar region ($Re = 2000$). The swirl flow was created by supplying air into three passages (one axial and two angular air supply on either sides).

They used varying swirl number ($Sw = 0.3,0.6,1.08$) with fixed H/D distance and reported that the flow acceleration and flow mixing near the impinging surface by swirl enhance the heat transfer whereas the

rising flow and the recirculating flow reduce the heat transfer. Ting Wang *et al.* (2005) experimentally studied the heat transfer performance of an array of impinging jet using liquid crystal technique (*Re* = 1039 - 51750) and interpreted the cross flow effects on the array of jet impingement heat transfer at fixed *H/D* distance. They reported that increased cross flow reduces the heat transfer rate and increases uniformity. Nuntadusit *et al.* (2012) examined the heat transfer and flow characteristics of swirling impinging jet using twisted tape inserts of swirl number *Sw* = 0,0.4,0.62,0.78 and 0.94 and reported that high heat transfer is obtained for Sw = 0.4 than circular impinging jet and it has diminished for larger swirl number (*Sw* = 0.78 and 0.94). Eiamsa-ard *et al.* (2015) investigated heat transfer characteristics of swirling jet with co and counter dual twisted tape inserts (CO-DSIJ and C-DSIJ) of varying twist ratio. They examined the effects of jet with Reynolds number range of 5000 - 20000 and H/D distance of 1 to 8 and reported that the heat transfer increased with increased twist ratio for CO-DSIJ and C-DSIJ without baffle and it was reverse for CO-DSIJ and C-DSIJ with baffle. Yan *et al.* (2004) carried out heat transfer study of array of elliptical impinging jet with the aspect ratio AR = 0.25,0.5,1,2,4 and Reynolds number = 1500, 3000 and 4500 and reporting that axial shift of impingement location occurs at aspect ratio AR > 1 and the axial shift at the upstream is due to inertia of jet while at the downstream is due to cross flow effect. Gioacchino *et al.* (2014) compared the heat transfer performance of impinging flow with fractal grid (grid with square pattern increasing at smaller scale) and regular square grid and concluded that fractal grid enhances heat transfer rate in the stagnation region at *H/D* ≤ 2 compared with regular grid and it decreases at larger plate distance (*H/D* > 4). The study by Mao (2005) compared round and swirling jets with impinging surface undergoing forced vibration on a vertical plane with the Reynolds number range of 440 - 27000 and *H/D* distance of 3 to 16. The study revealed that the stagnation Nusselt number increases with increasing amplitude of vibration of about 4% than no vibration case.

With respect to the literature review, the heat transfer characteristics of swirling flow has been analyzed either with swirl generator of single vane or multi vanes with varying swirl numbers. None of the previous studies have compared the heat transfer performance of impinging flow with varying number of guide vanes. To the authors' best knowledge this is the first experimental effort to examine the heat transfer characteristics of impinging jet using helicoid insert; the only contribution on this part is the numerical study by Sal B. Rodrigueza and Mohamed S. El-Genk (2010) on eliminating hot spots in reactor involving high temperature with quadruple helicoid insert, which creates radial and azimuthal momentum flow components resulting in extensive entrainment and mixing of surrounding gas. Thus in the present study, the heat transfer performance of impinging jet has been experimentally analyzed with helicoid inserts. The comprehensive study includes (1) six helicoid inserts of single vane, double vanes triple vanes (Sh, Dh, Th) having swirl numbers 0.75 and 1.1 each (2) Reynolds number range of 12700 - 32700 (3)

dimensionless nozzle exit to impinging surface distance of (H/D) 1- 4. The multi objective optimization method is employed to obtain optimal parameters for enhanced heat transfer performance and ANOVA test is performed to find influential parameters.

2. EXPERIMENTAL SETUP

The experimental setup is shown in Fig. 2. The air is drawn by a 1.5 HP high pressure blower and subsequently supplied to a smooth horizontal pipe through a heater and a venturi meter. The air temperature in the pipe is maintained at 35°C using heater and PID temperature controller with pt-100 temperature sensor. The flow rate of air is controlled by a flow regulating valve and its discharge is measured by the venturi meter connected with U tube manometer.
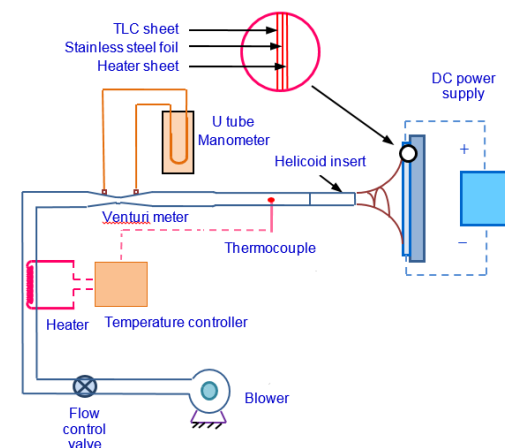

Fig. 2. Experimental setup.

The main pipe connecting upstream and downstream of the venturi meter has the length of 20 D and 15 D respectively to minimize fluctuations in flow past the bend and change in cross section. The pipe into which the swirl device inserted is smooth transition pipe (stainless steel) having an inner diameter of 31 mm and length of 830 mm. The outer surface of the pipe is insulated to minimize heat losses. The jet leaving the nozzle pipe impinges perpendicular to the surface as shown in Fig. 2. The impinging surface consists of an electric heater sheet, a thin stainless steel sheet and a TLC (thermo chromic liquid crystal) sheet. The stainless steel sheet has a size of 300 x 300 x 0.03 mm^3 and the TLC sheet has a size of 300 x 300 x 0.1 mm^3. The electric heater sheet and stain less steel sheet are clamped by screws over the surface of acrylic plate of size 450 x 450 x 12 mm^3. The TLC sheet is firmly pasted over the stain less steel foil ensuring no air gap and it is directly facing the impinging jet. A calibrated DC power unit (PSD 3203 - Scientific MesTechnik Ltd.) with voltage and current range of 0-30 V and 0-3 A respectively is used to supply uniform heat to impinging surface. A Canon camera (EOS 600D) is employed for obtaining the images of TLC. The swirl insert used in the current study consists of helicoid surface that wraps over the cylindrical part as shown in Fig.3. The first insert consists of single helicoid ribbon whereas the second and third kind of inserts having two and three helicoid ribbons that are spaced 180° and

120° apart respectively. These helicoid inserts are made of polymer by using rapid prototyping machine having the average surface roughness of 5μm.
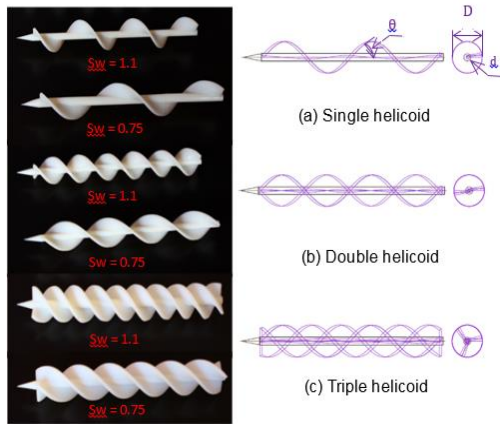

Fig.3. Helicoid inserts - Sw = 0.75 and 1.1.

The degree of swirl generated by the helicoid surfaces is determined by swirl number (*Sw*) which is given by Gupta *et al.* (1985)

$$Sw = \frac{2}{3} \left[\frac{1 - \dfrac{d^3}{D^3}}{1 - \dfrac{d^2}{D^2}} \right] \tan \phi \qquad (1)$$

where *D* is the outside diameter of helicoid vane, *d* is the diameter of helicoid vane hub and ϕ is angle of helicoid vane.

3. CALIBRATION OF TLC SHEET

The calibration rig consists of an acrylic plate (400 x 400 x 12 mm³), aluminium plate (300 x 300 x 3 mm³), heater and TLC sheets. Eight calibrated K- type thermocouples are placed on the grooves of the Aluminium plate by an adhesive acting as a thermally conductive paste. The thermocouples are connected to NI 9213 data acquisition system and the terminals of the heater are connected to the power supply unit as shown in Fig. 4.

Hallcrest (R35C1W) TLC sheets are used in this study. The bandwidth of the TLC defined by the Hallcrest is in temperature range between red start (35°C) and blue start (36°C). However, the bandwidth of TLC sheet is the range of temperature between red start (35°C) and clearing point temperature (49°C); while heating below 35°C, the sheet is black and when it reaches 35°C, it starts changing with red in color, between 35.2°C and 36°C it is green and blue in the range 36°C - 49°C. The aluminum plate is heated from 35°C to 48°C and its average temperature is measured via eight thermocouples located on the grooves. The color of the TLC and temperature of thermocouples are simultaneously recorded when the temperature reaches steady state. The normalized hue value with measured temperature are given in Fig. 5.
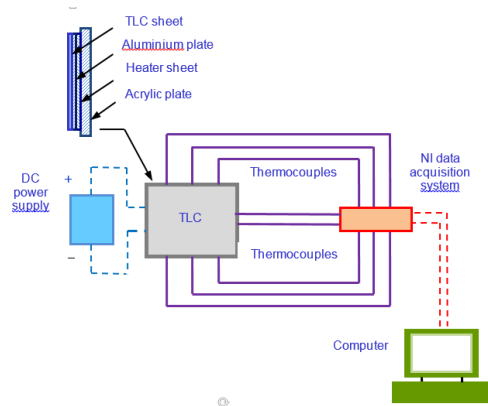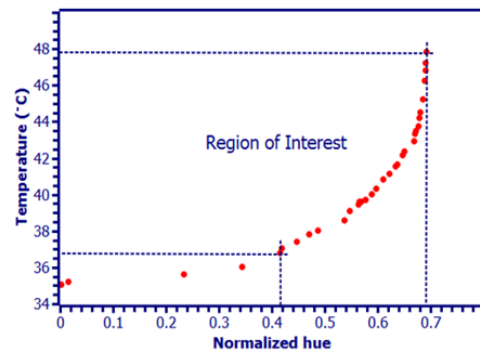

Fig.4. Schematic of calibration set up.

Fig.5. Temperature versus hue for calibration of TLC.

4. DATA REDUCTION

The temperature distribution of the impingement surface is recorded by a digital camera and the color pattern in RGB (red, green, blue) color domain is converted to HSI (hue, saturation, intensity) using image processing technique. According to Gonzalez *et al.* (2013), hue denotes pure color and saturation represents degree to which color is diluted by white light whereas intensity refers to brightness. In view of this, the normalized hue value of TLC versus temperature is plotted and presented in Fig.5. The change of color of TLC sheet is strongly related with temperature for the hue values ranging from 0.41 to 0.693 is considered to be the region of interest. A polynomial fit is used to correlate temperature with hue value. The hue value of TLC is converted into its surface temperature using the correlation. Considering the energy balance on the impinging surface, the heat transfer coefficient due to forced convection by the impinging jet and Nusselt number are evaluated using the Eqs. (2) and (3) respectively. It may be noted that the heat transfer coefficient is evaluated on different radius r with the predetermined center positioned at the intersection of axis of jet and impinging surface.

$$h = \frac{q_{in} - q_{cond} - q_{free\ conv} - q_{rad}}{(T_w(r) - T_j)} \qquad (2)$$

$$Nu = \frac{h\ D}{k_{air}} \qquad (3)$$

where q_{in} is the electrical power dissipating on the heated surface per unit area A, q_{cond} is the heat conduction per unit area in the stainless steel and TLC sheets, $q_{free\,conv}$ is the heat loss due to free convection per unit area and q_{rad} is the loss due to radiation per unit area. A is the area of stainless steel foil. $T_w(r)$ and T_j are the average temperature along circumferential direction on the impinging surface at radius r and jet exit temperature respectively, D is the inside diameter of pipe and k_{air} is thermal conductivity of air. q_{in} is evaluated by obtaining the magnitudes of voltage and current from DC power supply unit.

The heat conduction on the surfaces of stainless steel and TLC sheets (Eiamsa-ard *et al.,* 2015 and Geers *et al.,* 2008) due to temperature gradient is expressed as

$$q_{cond} = (k_{steel}\, t_{steel} + k_{TLC}\, t_{TLC})\left(\frac{\partial^2 T}{\partial x^2} + \frac{\partial^2 T}{\partial y^2}\right) \tag{4}$$

where k_{steel} and k_{TLC} are thermal conductivity of stainless steel and TLC sheets respectively and t_{steel} and t_{TLC} are thickness of stainless steel and TLC sheets respectively. x and y are the axes corresponding to surface of the sheets.

The heat loss due to free convection can be calculated from the expression

$$q_{free\,conv} = h_{free\,conv}\,(T_{sur} - T_a) \tag{5}$$

where $h_{free\,conv}$ is convective heat transfer coefficient of vertical surface obtained from empirical correlation given by Holman (2002), T_{sur} is average surface temperature and T_a is ambient temperature.

The radiation heat loss is given by the expression

$$q_{rad} = \sigma\, \epsilon_{TLC}\,(T_{sur}^4 - T_a^4) \tag{6}$$

Where, σ is the Stefan Boltzmann constant, ϵ_{TLC} is emissivity of TLC sheet (= 0.9 Geers *et al.* 2008). Based on the experimental results, the convection and radiation losses are estimated as 8.92% and 9.94% of total imposed heat flux whereas the heat loss due to conduction is 2.50% of total heat flux which are comparable with Eiamsa-ard *et al.* (2015). The heat transfer rate on the impinging surface is presented interms of Nusselt number versus dimensionless radial distance, *r/D*.

5. UNCERTAINTY ANALYSIS

An uncertainty analysis is performed using Kline-Mc Clintock method (Holman, 2007) and the equation used for calculating the uncertainty is given below

$$\Delta h= \left[\left(\frac{\partial h}{\partial Q}\right)^2(\epsilon_1)^2 + \left(\frac{\partial h}{\partial A}\right)^2(\epsilon_2)^2 + \left(\frac{\partial h}{\partial T_s}\right)^2(\epsilon_3)^2 + \left(\frac{\partial h}{\partial T_j}\right)^2(\epsilon_4)^2\right]^{\frac{1}{2}} \tag{7}$$

Where h, Q, A, T_s and T_j are the convective heat transfer coefficient, heat input, area of impinging surface, average temperature of the impinging surface and temperature at jet exit respectively and ϵ is the error in the measurement. The maximum uncertainty in the Nusselt number for single helicoid (Sw = 1.1) at H/D = 4 and r/D = 4.13 for Re = 12700 is 4.2%. The present estimates are based on 95% (20:1 odds) confidence level.

6. VALIDATION OF RESULTS

Since different types of swirl generators even with equal swirl strength do not have the same flow field farther downstream according to Gupta *et al.* (1985) and the selection of particular shape and type of swirling insert significantly affect the magnitude of heat transfer, the obtained experimental values of circular impinging jet are compared with the literature data. The Nusselt number values for Re = 23100 at r/D = 2 (calculated with $Re^{0.67}$ according to Goldstein *et al.,* 1986) presented for circular impinging jet are compared with previous studies (Dae *et al.* 2002, Yuan *et al.* 2006, Chung *et al.* 2005, Tadhg S. O. Donovon and Darina B. Murray, 2007) as shown in Fig.6 and a fairly good agreement can be seen.
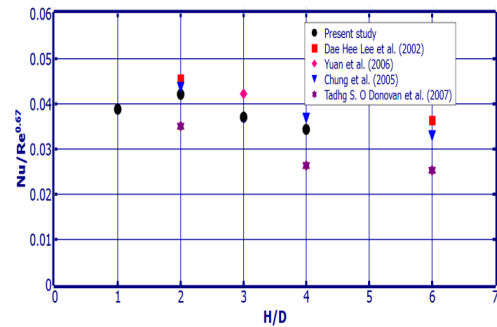
Fig. 6. Variation of *Nu/Re*$^{0.67}$ with *H/D* distance of CIJ for *Re* = 23100 at *r/D* = 2.

7. RESULTS AND DISCUSSION

7.1 Effect of helicoid vanes on Nusselt number distribution

Figures 7 and 8 show the radial Nusselt number distribution for circular jet (CIJ) and swirling impinging jet of Sw = 0.75 and 1.1 respectively for H/D = 1,2,3 and 4 at Reynolds number Re = 23100.

While comparing the heat transfer performance of CIJ and swirling jet as shown in Figs.7 and 8, the Nusselt number distribution for swirling jet is relatively higher than CIJ in the region $0 \le r/D \le 1.5$ at H/D = 1 (Figs. 7a and 8a). The increase in Nusselt
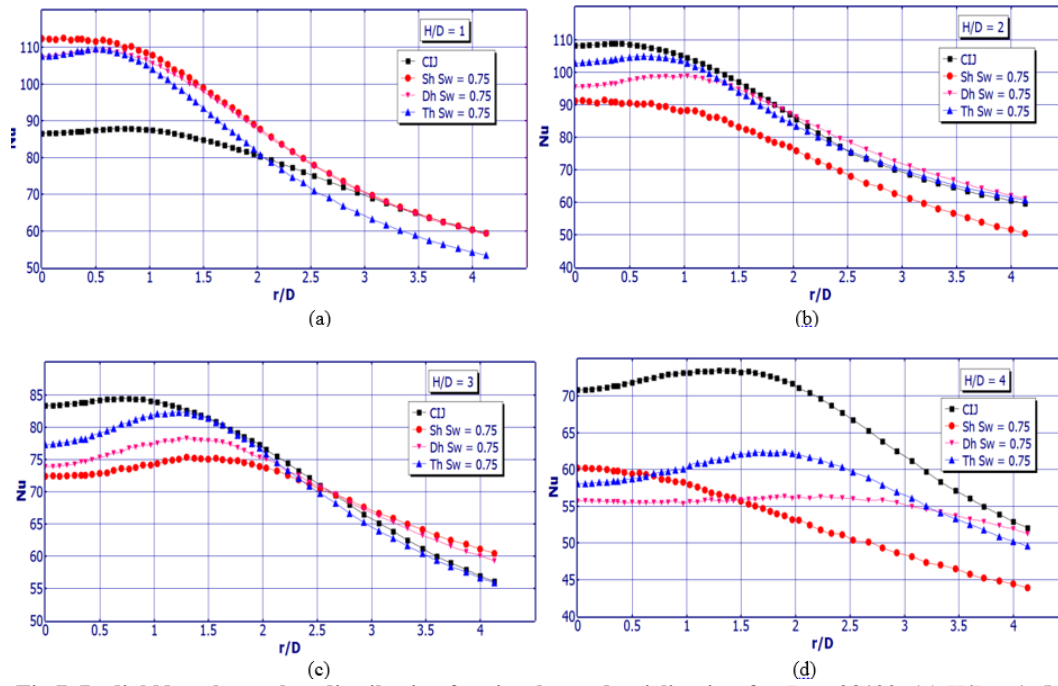
Fig.7. Radial Nusselt number distribution for circular and swirling jets for *Re* = 23100; (a) *H/D* = 1, (b) *H/D* = 2, (c) *H/D* = 3,   (d) *H/D* = 4.
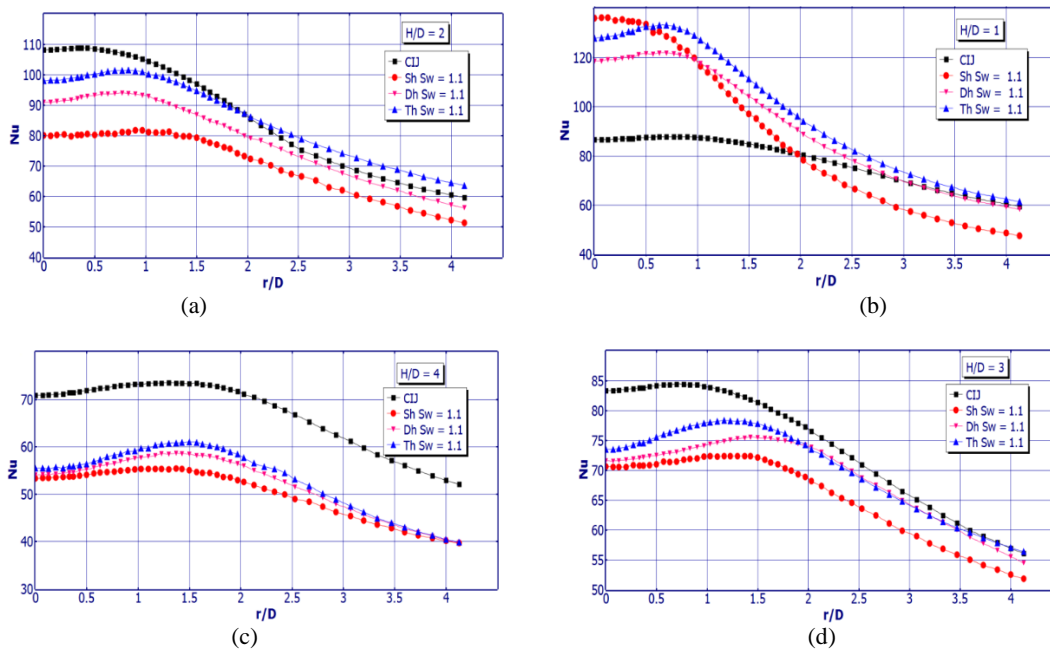
Fig. 8. Radial Nusselt number distribution for circular and swirling jets for *Re* = 23100; (a) *H/D* = 1,(b) *H/D* = 2, (c) *H/D* = 3,   (d) *H/D* = 4.

number at shorter *H/D* distance is partially related to an increase in exit velocity of the swirling jet due to reduction in flow area with the presence of insert as reported by Andrea Cardone (2012) causing higher turbulence, whereas lower intensity of turbulence at the exit of circular jet causing an increase in potential core length resulting in uniform velocity as reported by Viskanta (1993) and Alimohammadi *et al.* (2014). When the separation distance (*H/D* distance) increases the increase in Nusselt number in the impingement region is observed for CIJ compared

with swirling jet. This is due to the fact that the velocity of circular jet is uniform as the potential core length increases with increasing separation distance whereas enhanced mixing and turbulence due to interaction of swirling jet resulting in decrease of jet arrival velocity near the impinging surface. The swirling jet produces increased uniformity in heat transfer over the impinging surface with reduction in its magnitude compared with the circular jet at increased separation distances (H/D). The increased uniformity in heat transfer is due to the higher

spreading rate of swirling flow as assessed by Dae *et al. et al.* (2002).

The Nusselt number is higher in the region corresponding to $0 \le r/D \le 0.7$ for swirling flow of $Sw = 0.75$ at $H/D = 1$ as presented in Fig.7a. With minimal swirling effect at shorter H/D distance as reported by Andrea Cardone (2012), the increase in heat transfer in this region is due to increased mixing and turbulence of jet besides increased jet velocity at the exit as discussed earlier. The jet of the single helicoid maintains its original momentum with relatively lower spreading rate resulting in higher average Nusselt number distribution compared with double and triple helicoids. Beyond the region $r/D = 0.7$ the Nusselt number decreases radially due to the boundary layer development caused by an increase in velocity gradient resulting in reduction of Nusselt number.
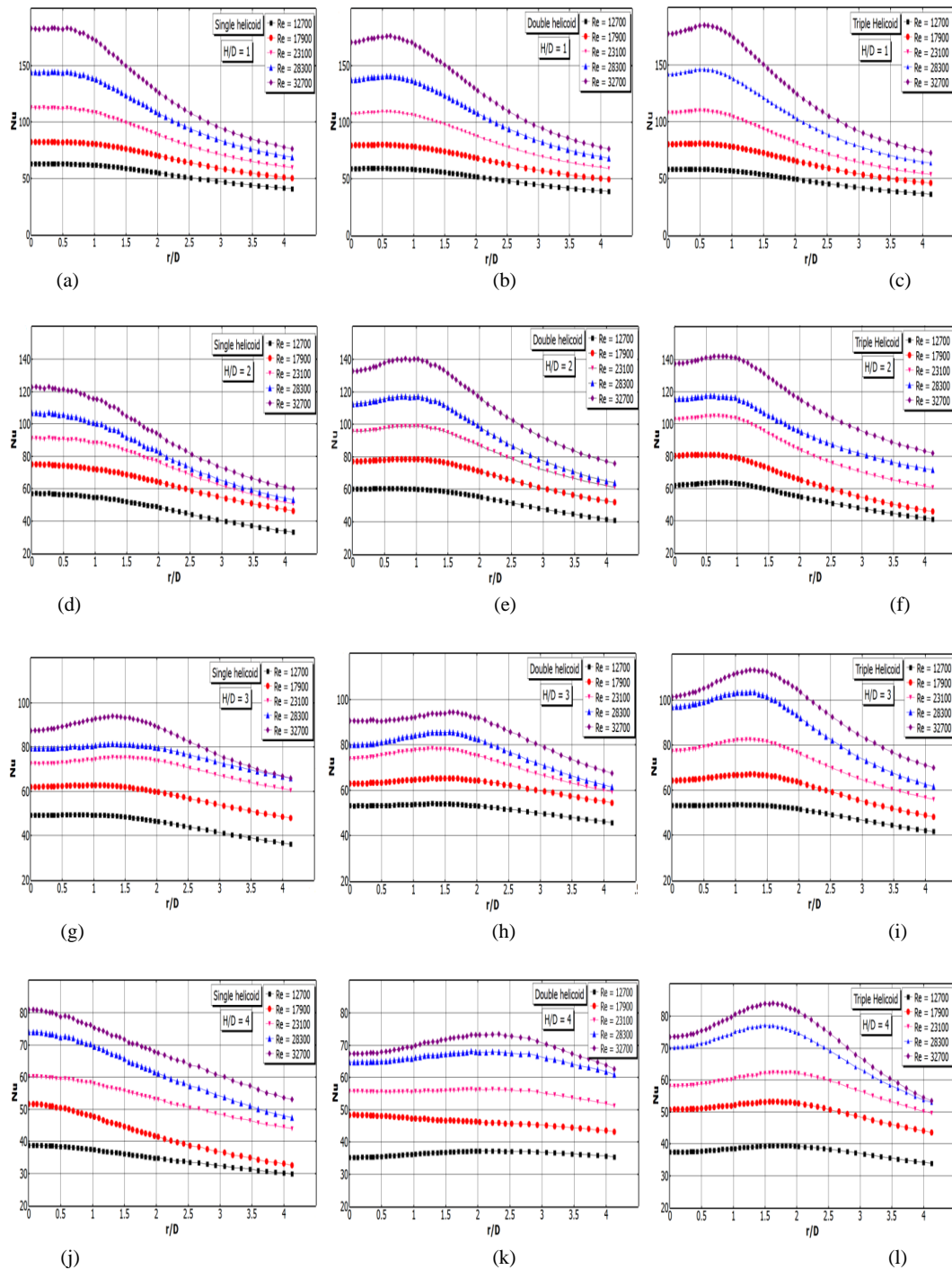
The average Nusselt number distribution of swirling jet over the impinging surface at $H/D = 2$ decreases compared with $H/D = 1$ as shown in Fig.7b for $Sw = 0.75$. This is attributed to the fact that the swirling jet losing its momentum when increasing the H/D distance as reported by Dae *et al. et al.* (2002) in their study for $Sw = 0.44$ and 0.77. The jet of triple helicoid insert produces relatively higher Nusselt number in the region corresponding to $0 \le r/D \le 1$ compared with single helicoid and double helicoid. This is due to the fact that the swirling effect of multiple vanes spreads the jet radially outward through the surrounding air while it approaches the impinging surface. This swirling effect and increased velocity on the outside surface of jet entrain relatively more surrounding air on the impinging surface increasing the heat transfer rate as reported by Huang and El-Genk (1998). The high flow velocity at the exit of the pipe is caused by reduction in the flow area due to the presence of helicoid insert as reported earlier. The average Nusselt number distribution of jet leaving with triple helicoid insert is 12.96%, 0.77% higher than single and double helicoid inserts respectively. The stagnation Nusselt number further reduces for swirling flow at $H/D = 3$ as presented in Fig.7c for $Sw = 0.75$. This is attributed to the fact that weakening of the axial flux of swirl momentum due to mixing of spreading jet at increased H/D distance as reported by Dae *et al. et al.* (2002). The Nusselt number is minimum at the stagnation region for $H/D = 3$ and increases radially reaching its maximum value at $r/D = 1.57, 1.3$ and 1.23 for single, double and triple helicoid inserts respectively. This is due to the fact that the swirling flow with high swirl number produces an axial pressure gradient near the exit of pipe that causes axial recirculation zone as reported by Andrea Cardone (2012). This phenomenon is known as vortex break down as stated by Panda and Mclaughlin (1994) and also shown by Yang *et al.* (2010) by PIV measurements.

The vortex break down (axial recirculation) causes low heat transfer zone at the centre of the impinging area resulting in lower stagnation Nusselt number as assessed by Andrea Cardone (2012) for $Sw = 0.8$. The increase in Nusselt number beyond the

stagnation region is due to higher spreading rate of the swirling flow with increased H/D distance. The result shows that the average Nusselt number distribution for triple helicoid is 15.5% and 12.9% higher than for single helicoid and double helicoid respectively at $H/D = 3$. This is due to the fact that the multiple jets of triple helicoid entrain relatively more ambient air on the impinging surface. It is observed from the results that the average Nusselt number distribution of swirling jet at $H/D = 3$ is lower than that of $H/D = 2$ at about 17.2%, 24.4% and 15.3% for single, double and triple helicoids respectively. It is due to the fact that reduced tangential momentum at increased nozzle exit to surface distances as reported earlier.

Figure 8 shows the Nusselt number distribution for swirling flow of $Sw = 1.1$ at $H/D = 1,2,3$ and 4. The result shows an increased Nusselt number for the swirling jet of $Sw = 1.1$ (Fig.8a) in the region $0 \le r/D \le 0.5$ when compared with $Sw = 0.75$ (Fig.7a) at $H/D = 1$. This is due to the fact that enhanced turbulence of jet at higher swirl. It is observed from the result that the swirl effect is evident at higher swirl causing entrainment of surrounding air by the jet leaving triple helicoid resulting in higher average Nusselt number distribution in the entire region. The phenomenon of vortex break down is observed for double and triple helicoids causing lower Nusselt number at the stagnation region and an increase gradually beyond this region till at $r/D = 0.63$ and 0.77 respectively. Besides stronger swirl, the swirling effect is more evident than $Sw = 0.75$ (Fig. 7b) in the impinging region with sufficient space for the jet leaving the nozzle pipe to spread at $H/D = 2$ as shown in Fig.8b for $Sw = 1.1$. The stronger swirl causes an axial pressure gradient resulting in vortex break down for the jet leaving double helicoid and triple helicoid. A significant decrease in stagnation Nusselt number is observed for the swirling impinging jet when compared with $H/D = 1$. This is attributed to the weakening of axial flux swirl momentum as discussed earlier.

The phenomenon of vortex breakdown is apparent for the swirling impinging jet at $H/D = 3$ causing lower Nusselt number at the stagnation region and an increase till at $r/D \approx 1.1, 1.43$ and 1.23 respectively as presented in Fig.8c for $Sw = 1.1$. The swirling jet of triple helicoid entrains more ambient air on the impinging surface resulting in relatively higher value of Nusselt number compared with single helicoid and double helicoid as reported earlier. The effect of swirl is rarely seen beyond the region $r/D = 3.5$ (Dae *et al. et al.* 2002 and Bakirci and Bilen 2007). The average Nusselt number distribution of single, double and triple helicoids reduces by 2.4%, 13.7% and 16.5% than $H/D = 2$. This is due to the fact that the lower tangential momentum at increased H/D distance as reported earlier. While increasing the nozzle exit to impinging surface distance (H/D = 4), the swirling jet broadens the impinged area with further reduction in Nusselt number compared with $H/D = 3$ as shown in Fig.8d for $Sw = 1.1$. At higher swirl, the strong swirl momentum of jet leaving

Fig.9. Radial Nusselt number distribution at H/D = 1,2,3 and 4 for swirling jet of Sw = 0.75.

single helicoid of *Sw* = 1.1 causes higher spreading rate resulting in uniform distribution of Nusselt number in the region corresponding to $0 \leq r/D \leq 2$ whereas there is no uniformity for single helicoid of *Sw* = 0.75 probably due to lower swirl momentum causing mixing of spreading jet at *H/D* = 4. Figure 8d shows that the axial pressure gradient becomes stronger with increased swirl number compared with *Sw* = 0.75 (Fig. 7d) as reported by Andrea Cardone (2012) causing axial recirculation zones for the swirling jet.

7.2 Effect of Number of Helicoid Vanes on Varying Reynolds Number

Figure 9 presents the Nusselt number variations for the swirling jet for the Reynolds number range of 12700 - 32700 at H/D = 1, 2, 3 and 4. The Nusselt number increases with increase in Reynolds number at all radial positions. The increase in Nusselt number with increasing Reynolds number for the same H/D distance is associated with corresponding increase in jet arrival velocity at the target surface.

The Nusselt number value at the stagnation region is maximum for single helicoid for the given Reynolds number at H/D = 1 (Fig.9a) and it decreases for increasing radial distance and the Nusselt number is highest in the stagnation region for the double and triple helicoids (Fig. 9b and 9c) for Re = 12700, 17900 and 23100 whereas the phenomenon of vortex breakdown is observed for double and triple helicoids for Re = 28300 and 32700 causing lower Nusselt number at the stagnation region and marginally increases till at r/D = 0.5 - 0.63 as the jets spread. A Steep decrease in Nusselt number beyond the stagnation region is observed for single helicoid at H/D = 2 (Fig.9d). This is more intense for Re = 28300 and 32700. The phenomenon of vortex break down is evident for double and triple helicoids (Figs. 9e and 9f) for Re = 32700 causing lower Nusselt number at the stagnation region with a marginal increase at r/D ≈ 1 and r/D ≈ 0.83 respectively. The impinging area is more broadened thereby increasing the uniformity of Nusselt number distribution at H/D = 3 as shown in Fig. 9g, 9h and 9i. This is probably due to strong swirl momentum with sufficient separation distance resulting in higher spreading rate of flow. The Nusselt number peak is observed for the swirling jet and the peak is more intense when the Reynolds number increases as shown in Fig. 9g, 9h and 9i. Moreover, the triple helicoid produces more steep rise in Nusselt number from the stagnation region compared with single helicoid and double helicoid. This is due to the intense axial pressure gradient caused by strong swirl resulting in axial recirculation zone as reported earlier. When increasing the separation distance further (H/D = 4), there is a steep fall in the Nusselt number distribution from the stagnation region causing non uniform heat transfer over the impinging surface for single helicoid jet as shown in Fig.9j. This is due to the jet leaving the single helicoid losing its momentum with increased separation distance causes mixing of spreading jet resulting in non uniform distribution of Nusselt number as reported earlier and it is more intense at higher Reynolds number. On the contrary, the jets leaving double helicoid with strong swirl momentum cause higher spreading rate producing relatively more uniform cooling as shown in Fig. 9k. The strong swirl effect of jet leaving triple helicoid causes axial pressure gradient resulting in vortex break down and it is more intense at Reynolds numbers 28300 and 32700 at H/D = 4 as shown in Fig. 9l.

8. OPTIMIZATION USINGPRINCIPLE COMPONENT ANALYSIS

Principle component analysis is a multivariate technique which is applied when interdependence exists among the set of variables, (Miszczyk and Kazimierz Darowicki 2016) summarizes the information present in the existing variables interms of smaller number of uncorrelated groupings with minimum data loss (Manwendra K. Tripathi et al. 2015 and Elangovan et al. 2011). It develops first principle component accounting the largest variation in the data set (Lee Ing Tong et al. 2005) and subsequent components account for as much of the

remaining variance as possible. In order to obtain optimal performance of swirling jet, the experimental values are employed in a multi objective optimization technique of principle component analysis.

The experimental design matrix of 72 trials is obtained by considering four levels of one parameter, two levels of another parameter and three levels for rest of the parameters as given in Table 1.

Table 1 Parameters selected for experimentation

Parameter	Level 1	Level 2	Level 3	Level 4
Swirl Number	Sw = 0.75	Sw = 1.1	-	-
Re Number	12700	23100	32700	-
H/D Ratio	1	2	3	4
Helicoid Vanes	Single	Double	Triple	-

Nusselt number decay, non uniformity index (calculated according to Ting Wang *et al.* 2005) and average Nusselt number distribution are the experimental values of the selected parameters in this study. The Signal to Noise (S/N) ratio is considered to formulate smaller the better and larger the better concepts as the Nusselt number decay and non uniformity index are desired to be lower and the average Nusselt number distribution to be higher to meet the optimal performance. The normalizing sequence of S/N ratio is obtained before carrying out principle component analysis.

The S/N ratio of the response is calculated using the Eqs. (8) and (9)

Smaller the better :

$$S/N = -10 \log \left[\frac{1}{N} \sum_{i=1}^{N} s_i^2 \right] \tag{8}$$

Larger the better :

$$S/N = -10 \log \left[\frac{1}{N} \sum_{i=1}^{N} \frac{1}{s_i^2} \right] \tag{9}$$

where *N* is number of experimental samples and s_i is measured *i*th sample.

The method involved in the principle component analysis is given below.

Step 1: Developing measured multiple response array

$$Y = \begin{bmatrix} y_{11} & y_{12} & \cdots & y_{1n} \\ y_{21} & y_{22} & \cdots & y_{2n} \\ y_{21} & y_{22} & \cdots & y_{3n} \\ \vdots & \vdots & \vdots & \vdots \\ y_{m1} & y_{m2} & \cdots & y_{mn} \end{bmatrix} \tag{10}$$

Table 2 Eigenvectors and proportion of principle components

Components	Eigenvalue	Proportion %	Cumulative %	Eigenvector [$Nu_{decay}, \xi, Nu_{avg}$]
Component 1	2.2453	74.80	74.80	[0.577, 0.630, -0.520]
Component 2	0.5860	19.50	94.40	[0.579, 0.133, 0.804]
Component 3	0.1687	5.60	100	[-0.576, 0.765, 0.288]
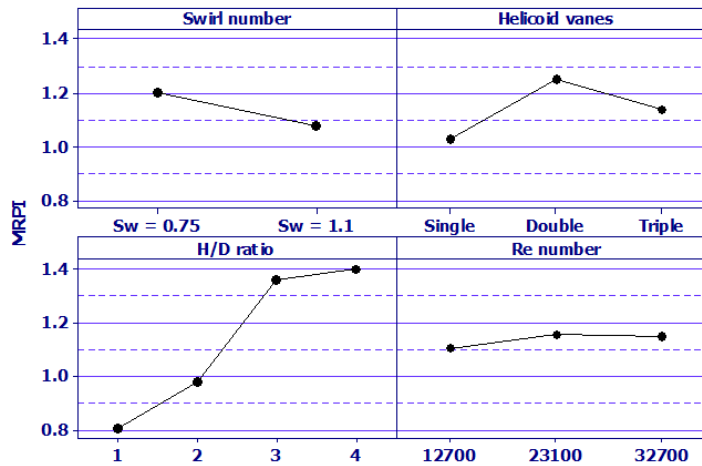
Fig.10. Main effects Plot for MRPI.

Where y is Normalized Signal to Noise ratio of measured responses, m the number of experimental trial and n is the number of responses.

Step 2: Evaluating correlation coefficient - The correlation matrix S is obtained by evaluating correlation coefficient as given by

$$s_{p,q} = \frac{Cov[y_i(p), y_i(q)]}{\sigma[y_i(p)] \cdot \sigma[y_i(q)]} \tag{11}$$

where $Cov[y_i(p), y_i(q)]$ is sequence covariance of $y_i(p)$ and $y_i(q)$, $\sigma[y_i(p)]$ is the standard deviation of $y_i(p)$ sequence and $\sigma[y_i(q)]$ is the standard deviation of $y_i(q)$ sequence.

Step 3 : Computing eigenvalues λ and eigenvectors $\vec{V}_{ik}$ from the correlation array

The values of λ can be found by satisfying the characteristic equation of the matrix S

$$\det(S - \lambda I) = 0 \tag{12}$$

where I is the identity matrix.

The eigenvectors $\vec{V}_{ik}$ can be calculated by solving the following equation

$$(S - \lambda I)\vec{V}_{ik} = 0 \tag{13}$$

where, $\vec{V}_{ik} = [v_{k1} \ v_{k2} ... v_{kn}]^T$ and $k = 1,2,3...n$

Step 4 : Determination of principle component - The uncorrelated principle component is evaluated as follows

$$\beta_{mk} = \sum_{i=1}^{n} y_{mi} \cdot \vec{V}_{ik} \tag{14}$$

The first principle component is β_{m1} and the second principle component is β_{m2} (Kamran Zeinalzadeha and Elnaz Rezaeib, 2017) and so on.. With respect to the variance, the principle components are arranged in descending order and first principle component β_{m1} accounts for large part of the variance.

The principle component analysis is carried out as discussed in this section. The eigenvalues and the corresponding eigenvectors are evaluated with their percentage proportions given in Table 2. The principle component of each response is determined using the Eq. (14) and subsequently the multiple response performance index (MRPI) is obtained by adding up all the principle components (Saurav Datta *et al.* 2009) for each trial.. The optimum parameter level is determined by calculating the average value MRPI for each individual parameter and is given Table 4.

The main effect plot for MRPI (Fig.10) shows that its magnitude increases with increase in *H/D* ratio and it is marginal for increase in Reynolds number whereas the value of MRPI decreases with increase in swirl number. The MRPI is relatively higher for the double helicoid vanes compared with rest of the

Table 3 Design Matrix of Experimental data and Principle Component values

Trial No	Swirl	Vanes	H/D ratio	Re	Experimental values			Principle component			MRPI
					Nu number decay Nu_{decay}	Non uniformity Index ξ	Avg. Nu number Nu_{avg}	Nu number decay Nu_{decay}	Non uniformity Index ξ	Avg. Nu number Nu_{avg}	
1	0.75	single	1	12700	0.114	0.132	55.54	0.175	0.561	0.177	0.913
2	0.75	single	1	23100	0.173	0.196	92.94	0.120	0.365	0.366	0.851
3	0.75	single	1	32700	0.230	0.269	140.50	0.081	0.208	0.517	0.806
4	0.75	single	2	12700	0.140	0.155	49.02	0.148	0.481	0.131	0.760
5	0.75	single	2	23100	0.146	0.171	77.77	0.142	0.432	0.300	0.874
6	0.75	single	2	32700	0.195	0.216	98.66	0.104	0.318	0.388	0.810
7	0.75	single	3	12700	0.063	0.091	46.01	0.255	0.748	0.108	1.111
8	0.75	single	3	23100	0.014	0.066	64.38	0.458	0.906	0.231	1.595
9	0.75	single	3	32700	0.019	0.098	85.63	0.415	0.710	0.336	1.461
10	0.75	single	4	12700	0.085	0.078	35.38	0.215	0.824	0.012	1.051
11	0.75	single	4	23100	0.099	0.095	54.18	0.194	0.728	0.168	1.090
12	0.75	single	4	32700	0.136	0.123	69.89	0.151	0.598	0.261	1.010
13	0.75	double	1	12700	0.107	0.128	52.58	0.184	0.576	0.157	0.917
14	0.75	double	1	23100	0.148	0.187	91.38	0.140	0.388	0.360	0.888
15	0.75	double	1	32700	0.187	0.249	138.52	0.109	0.247	0.512	0.868
16	0.75	double	2	12700	0.086	0.115	54.97	0.213	0.633	0.173	1.019
17	0.75	double	2	23100	0.087	0.143	87.17	0.211	0.522	0.342	1.075
18	0.75	double	2	32700	0.105	0.182	118.83	0.186	0.401	0.456	1.043
19	0.75	double	3	12700	0.019	0.046	52.03	0.412	1.092	0.153	1.657
20	0.75	double	3	23100	0.014	0.077	72.86	0.460	0.829	0.277	1.566
21	0.75	double	3	32700	0.034	0.089	87.42	0.338	0.758	0.343	1.439
22	0.75	double	4	12700	0.007	0.019	36.24	0.556	1.528	0.021	2.105
23	0.75	double	4	23100	0.007	0.021	55.29	0.558	1.481	0.175	2.214
24	0.75	double	4	32700	0.006	0.039	69.72	0.580	1.165	0.260	2.005
25	0.75	triple	1	12700	0.125	0.145	50.64	0.163	0.516	0.143	0.822
26	0.75	triple	1	23100	0.183	0.222	87.80	0.112	0.304	0.345	0.761
27	0.75	triple	1	32700	0.212	0.281	139.75	0.093	0.186	0.515	0.794
28	0.75	triple	2	12700	0.102	0.122	55.36	0.191	0.603	0.176	0.970
29	0.75	triple	2	23100	0.143	0.167	87.85	0.145	0.445	0.345	0.935
30	0.75	triple	2	32700	0.126	0.166	119.80	0.161	0.449	0.459	1.069
31	0.75	triple	3	12700	0.045	0.073	50.68	0.299	0.857	0.144	1.300
32	0.75	triple	3	23100	0.037	0.111	74.40	0.326	0.649	0.284	1.259
33	0.75	triple	3	32700	0.018	0.134	99.47	0.422	0.554	0.391	1.367
34	0.75	triple	4	12700	0.011	0.039	37.78	0.483	1.169	0.036	1.688
35	0.75	triple	4	23100	0.009	0.058	58.75	0.518	0.969	0.198	1.685
36	0.75	triple	4	32700	0.007	0.115	74.79	0.545	0.629	0.286	1.460
37	1.1	single	1	12700	0.113	0.134	55.45	0.176	0.555	0.177	0.908
38	1.1	single	1	23100	0.302	0.329	94.87	0.045	0.107	0.373	0.525
39	1.1	single	1	32700	0.358	0.408	143.94	0.022	0.000	0.526	0.548
40	1.1	single	2	12700	0.424	0.133	46.11	0.000	0.559	0.109	0.668
41	1.1	single	2	23100	0.090	0.135	72.84	0.208	0.551	0.276	1.035
42	1.1	single	2	32700	0.058	0.129	85.33	0.266	0.575	0.334	1.175
43	1.1	single	3	12700	0.022	0.051	43.96	0.397	1.032	0.091	1.52
44	1.1	single	3	23100	0.051	0.097	67.02	0.282	0.714	0.246	1.242
45	1.1	single	3	32700	0.073	0.107	77.38	0.236	0.668	0.299	1.203
46	1.1	single	4	12700	0.056	0.143	34.26	0.269	0.523	0.000	0.792
47	1.1	single	4	23100	0.038	0.095	51.26	0.320	0.724	0.148	1.192
48	1.1	single	4	32700	0.026	0.064	76.26	0.372	0.922	0.293	1.587
49	1.1	double	1	12700	0.105	0.133	54.28	0.186	0.557	0.169	0.912
50	1.1	double	1	23100	0.179	0.230	97.33	0.115	0.285	0.383	0.783
51	1.1	double	1	32700	0.187	0.283	147.29	0.109	0.182	0.535	0.826
52	1.1	double	2	12700	0.086	0.109	51.36	0.213	0.657	0.148	1.018

53	1.1	double	2	23100	0.104	0.151	81.48	0.188	0.496	0.318	1.002
54	1.1	double	2	32700	0.079	0.137	99.22	0.224	0.545	0.390	1.159
55	1.1	double	3	12700	0.039	0.057	43.42	0.317	0.978	0.087	1.382
56	1.1	double	3	23100	0.032	0.062	64.94	0.345	0.935	0.234	1.514
57	1.1	double	3	32700	0.120	0.170	77.12	0.168	0.437	0.297	0.902
58	1.1	double	4	12700	0.021	0.154	36.28	0.400	0.487	0.021	0.908
59	1.1	double	4	23100	0.015	0.105	53.28	0.450	0.678	0.162	1.29
60	1.1	double	4	32700	0.011	0.082	68.28	0.483	0.801	0.253	1.537
61	1.1	triple	1	12700	0.108	0.137	56.29	0.183	0.527	0.182	0.892
62	1.1	triple	1	23100	0.184	0.242	104.36	0.111	0.243	0.408	0.762
63	1.1	triple	1	32700	0.225	0.317	163.14	0.085	0.126	0.572	0.783
64	1.1	triple	2	12700	0.101	0.131	62.95	0.192	0.536	0.223	0.951
65	1.1	triple	2	23100	0.096	0.146	87.35	0.198	0.512	0.343	1.053
66	1.1	triple	2	32700	0.097	0.163	112.69	0.197	0.458	0.436	1.091
67	1.1	triple	3	12700	0.030	0.056	42.47	0.354	0.977	0.079	1.410
68	1.1	triple	3	23100	0.022	0.094	71.93	0.398	0.731	0.272	1.401
69	1.1	triple	3	32700	0.016	0.126	89.83	0.434	0.426	0.353	1.213
70	1.1	triple	4	12700	0.019	0.161	38.74	0.416	0.440	0.045	0.901
71	1.1	triple	4	23100	0.013	0.114	54.74	0.461	0.584	0.172	1.217
72	1.1	triple	4	32700	0.010	0.081	76.74	0.506	0.711	0.296	1.513

Table 4 Average MRPI for various Parameters

Parameter	Level 1	Level 2	Level 3	Level 4	Max-Min	Ranking
Swirl Number	1.201	1.078	-	-	0.123	3
Re Number	1.107	1.1588	1.1530	-	0.051	4
H/D Ratio	0.809	0.984	1.363	1.402	0.593	1
Helicoid Vanes	1.030	1.251	1.137	-	0.221	2

Table 5 ANOVA results for MRPI

Factors	DOF	SS	MS	F value	P value	% contribution
Swirl Number	1	0.2721	0.2721	5.190	0.026	3.11
Helicoid Vanes	2	0.5863	0.2931	5.590	0.006	6.70
H/D Ratio	3	4.5494	1.5165	28.930	0.000	52.00
Re Number	2	0.0381	0.0191	0.360	0.697	0.44
Error	63	3.3029	0.0524	-	-	37.75
Total	71	8.7487	-	-	-	100.00

vanes. Fig. 11 shows the interaction plot obtained from average MRPI of each parameter. The influence of a parameter over rest of the parameters can be identified by an interaction plot as shown by Senthilkumar *et al.* (2014). The non parallel lines in the interaction graph between *H/D* ratio, number of vanes and swirl number depict significant relation among these parameter. The MRPI is relatively higher for double helicoid vanes and it increases with an increase in *H/D* ratio for the specified Reynolds number whereas it decreases with an increase in swirl number as shown in Fig.11. The MRPI increases with an increase in Reynolds number for

the given number of vanes (Fig.11) and decreases with an increase in swirl number. In addition, the MRPI increases for double and triple helicoid with increase in *H/D* ratio whereas it decreases for single helicoid at *H/D* ratio of 4.

The MRPI is relatively higher for double helicoid vanes for the given swirl number and it increases with *H/D* ratio for *Sw* = 0.75 and marginally reduces at *H/D* ratio of 4 for *Sw* = 1.1.

The ANOVA and F test (Rudolf J. Freund *et al.* 2006) are performed to validate the   model adequacy. The terms of the model are statistically
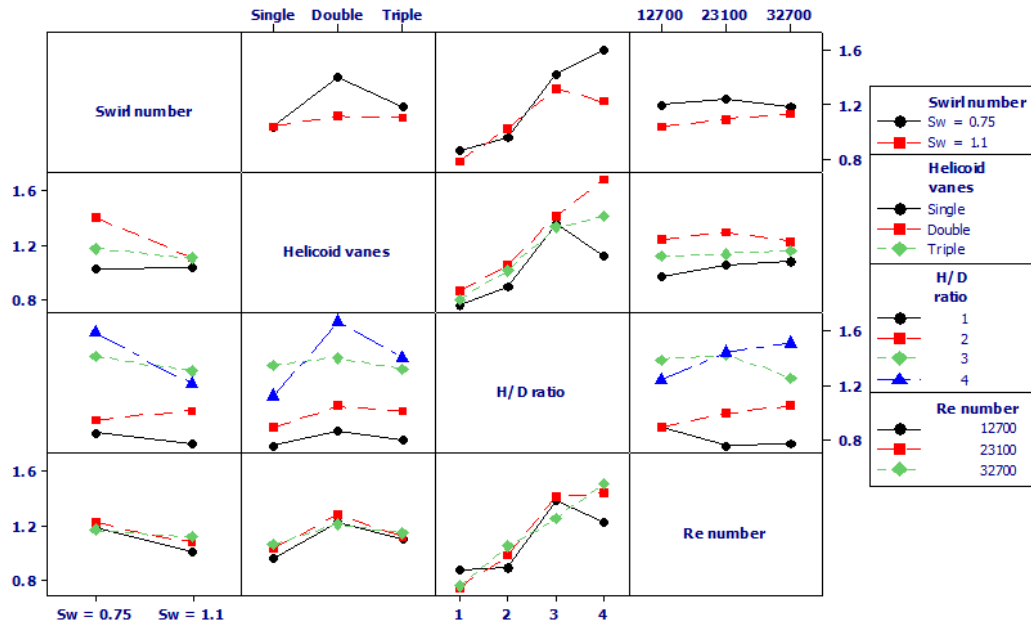
Fig. 11. Interaction Plot for MRPI.

significant when their P values are less than 0.05 owing to the chosen 95% confidence level. The lower the P values (< 0.05) of *H/D* ratio, number of helicoid vanes and swirl number substantiate their statistical significance whereas the $P > 0.05$ indicates nominal significance of *Re* number as shown in Table 5. The F statistic compares the variance between the groups to the variance within the groups by taking the ratio of mean sum of squares to the error mean sum of squares. The higher F value for the *H/D* ratio shows that the variability is relatively large within group variability meaning their significant effect. The percentile contribution of individual parameter over the computed MRPI is identified from the ANOVA results and presented in Table 5. The *H/D* ratio is the higher influencing parameter. In the order of ranking *H/D* ratio, number of helicoid vanes and swirl number are the influencing parameters.

9. CONCLUSION

An experimental investigation has been performed for studying the heat transfer characteristics of swirling and circular impinging jet on the flat surface. The multi objective optimization technique is used to analyze the experimental values. The following conclusions have been drawn

- By increasing the *H/D* distance, the swirling flow produces relatively more uniform cooling with reduction in magnitude when compared with circular impinging jet.

- The swirl effect is minimal in the region $0 \leq r/D \leq 0.7$ at shorter *H/D* distance (*H/D* =1) for *Sw* = 0.75 and the heat transfer enhancement is due to increased turbulence and mixing of jet besides an increased jet velocity at exit whereas it is significant for *Sw* = 1.1.

- The swirl effect and high flow velocity at the exit of triple helicoid entrain more ambient air on the impinging surface producing of higher average Nusselt number distribution compared with single and double helicoids of *Sw* = 0.75 and 1.1 at *H/D* = 2,3 and 4

- The heat transfer peaks are more intense at higher Reynolds number in the stagnation region due to higher tangential component of velocity of the swirling jet and significantly move away in radial direction from the axis of the jet when the separation distances increases.

- The presence of axial recirculation zone marginally affects the uniformity of Nusselt number distribution for the double and triple helicoids at high swirl number (*Sw* = 1.1) at *H/D* = 4 and it is evident for triple helicoids for *Sw* = 0.75 and 1.1 at *H/D* distance of 2,3 and 4 causing lower Nusselt number at the stagnation region.

- The principle component analysis reveals that the performance index is relatively higher for double helicoid of *Sw* = 0.75 with higher *H/D* ratio and the ANOVA result shows that the *H/D* ratio contributes 52% on the output.

REFERENCES

Alimohammadi, S., Darina B. M. and T. Persoons. (2014). Experimental Validation of a Computational Fluid Dynamics Methodology for Transitional Flow Heat Transfer Characteristics of a Steady Impinging Jet.*Journal of Heat Transfer* 136, 1-9.

Andrea I. and G. Cardone (2012). Heat transfer rate and uniformity in multichannel swirling

impinging jets. *Applied Thermal Engineering* 49, 89-98.

Bakirci, K. and K. Bilen (2007). Visualization of heat transfer for impinging swirl flow. *Experimental Thermal and Fluid Science* 32, 182–191.

Chung, Y.S., D. H. Lee and P. M. Ligrani (2005). Jet Impingement Cooling of chips equipped with cylindrical pedestal profile fins. *Journal of Electronic Packaging* ASME 127, 106-112.

Dae, H. L., J. Song and M. Chan Jo (2004). The Effects of Nozzle Diameter on Impinging Jet Heat Transfer and Fluid Flow. *Journal of Heat Transfer*ASME 126, 554-557.

Dae, H. L., S. Youl Won, Y. Taek Kim and Y. Suk Chung. (2002). Turbulent heat transfer from a flat surface to a swirling round impinging jet. *International Journal of Heat and Mass Transfer* 45, 223-227.

Doncaster, C. P. and A. J. H. Davey (2007). Analysis of Variance and Covariance: How to Choose and Construct Models for the Life Sciences. Cambridge University Press.

Eiamsa-ard, S., K. Nanan and K. Wongcharee (2015). Heat transfer visualization of co/counter-dual swirling impinging jets by thermo chromic liquid crystal method. *International Journal of Heat and Mass Transfer* 86, 600–621.

Elangovan, M., S. Babu Devasenapati, N. R. Sakthivel and K. I. Ramachandran (2011). Evaluation of expert system for condition monitoring of a single point cutting tool using principle component analysis and decision tree algorithm. *Expert Systems with Applications* 38, 4450‑4459.

Fenot, M., E. Dorignac and G. Lalizel (2015). Heat transfer and flow structure of a multichannel impinging jet. *International Journal of Thermal Sciences* 90, 323-338.

Geers, L. F. G., M. J. Tummers, T. J. Bueninck and K. Hanjalic (2008). Heat transfer correlation for hexagonal and in-line arrays of impinging jets. *International Journal of Heat and Mass Transfer* 51, 5389–5399.

Gioacchino C., S. Discetti and T. Astarita (2014). Heat transfer enhancement of impinging jets with fractal generated turbulence. *International Journal of Heat and Mass Transfer* 75, 173 - 183.

Goldstein, R. J., A. I. Behbahani and K. Kieger Heppelmann (1986). Stream wise distribution of the recovery factor and the local heat transfer coefficient to an impinging circular air jet. *International Journal of Heat and Mass Transfer* 29, 1227-1235.

Gonzalez, R. C., R. E. Woods and S. L. Eddins (2013). Digital Image Processing using

MATLAB. Second edition, McGraw Hill education, India.

Gupta, A. K., D. G. Lilley and N. Syred (1985). *Swirl Flows*. Abacus Press, Cambridge.

Holman, J. P. (2002). *Heat transfer*, Eight SI metric edition, Tata McGraw- Hill. India

Holman, J. P. (2007). *Experimental Methods for Engineers*, Seventh edition McGraw Hill Education. India

Huang, L. and M.S. El-Genk (1998). Heat transfer and flow visualization experiments of swirling, multi-channel and conventional impinging jets. *International Journal of Heat and Mass Transfer* 41, 583-600.

Kamran Zeinalzadeha and Elnaz Rezaeib (2017). Determining spatial and temporal changes of surface water quality using principal component analysis. *Journal of Hydrology: Regional Studies* 13, 1-10.

Koichi I. and K. Tsukamoto (2010). Heat Transfer Characteristics of a Swirling Laminar Impinging Jet. *Journal of Heat Transfer- ASME* 132, (012201) -1-5

Lee Ing Tong, Chung HoWang and Hung Cheng Chen (2005). Optimization of multiple responses using principal component analysis and technique for order preference by similarity to ideal solution. *International Journal of Advanced Manufacturing Technology* 27, 407-414.

Luai M. Al-Hadhrami (2010). Study of Heat Transfer Distribution in a Channel with Inclined Target Surface Cooled by a Single Array of Staggered Impinging Jets. *Heat Transfer Engineering* 31, 234–242.

Manwendra K. Tripathi., P.P. Chattopadhyay and Subhas Ganguly (2015). Multivariate analysis and classification of bulk metallic glasses using principal component analysis. *Computational Materials Science* 107, 79‑87.

Mao, Y. W., (2005). Flow structures and heat transfer of swirling jet impinging on a flat surface with micro-vibrations. *International Journal of Heat and Mass Transfer* 48, 545-560.

Miszczyk and Kazimierz Darowicki (2016). Determination of time dependence of coated metal electrical and electrochemical parameters during exposure using principal component analysis. *Progress in Organic Coatings* 96, 80-87.

Nuntadusit, C., M. Waehayee, A. Bunyajitradulya and S. Eiamsa-ard (2012). Visualization of flow and heat transfer characteristics for swirling impinging jet. *International Communications in Heat and Mass Transfer* 39, 640–648.

Panda, J. and D. K. Mclaughlin (1994). Experiments on the instabilities of a swirling jet. *Physics of fluids* 6, 263-276.

Rudolf J. Freund ,William J. Wilson and Ping Sa (2006). *Regression Analysis*, Second edition, Elsevier Academic Press.

Sal, B. Rodrigueza and M. S. El-Genk. (2010). Numerical investigation of potential elimination of hot streaking and stratification in the VHTR lower plenum using helicoid inserts. *Nuclear Engineering and Design* 240, 995–1004.

Saurav Datta, Goutam Nandi, Asish Bandyopadhyay and Pradip Kumar Pal (2009). Application of PCA-based hybrid Taguchi method for correlated multicriteria optimization of submerged arc weld: a case study. *International Journal of Advanced Manufacturing Technology* 45, 276–286.

Senthilkumar, N., T. Tamizharasan and V. Anandakrishnan (2014). Experimental investigation and performance analysis of cemented carbide inserts of different geometries using Taguchi based grey relational analysis. *Measurement* 58, 520–536.

Tadhg S. O. Donovon, Darina B. Murray (2007). Jet Impingement heat transfer -Part I: mean and root mean square heat transfer and velocity distributions. *International Journal of Heat transfer* 50, 3291-3301.

Ting, W., M. Lin and R. S. B. (2005). Flow and heat transfer of confined impingement jets cooling using a 3-D transient liquid crystal scheme. *International Journal of Heat and Mass Transfer* 48, 4887–4903.

Viskanta, R. (1993). Heat Transfer to Impinging Isothermal Gas and Flame Jets. Experimental *Thermal and Fluid Science* 6, 111-134.

Wae-Hayee, M., P. Tekasakul, S. Eiamsa-ard and C. Nuntadusit (2015). Flow and heat transfer characteristics of inline impinging jets with cross flow at short jet-to-plate distance. *Experimental Heat Transfer* 28, 511–530.

Yan, W. M., S. C. Mei, H. C. Liu, C. Y. Soong and W. J. Yang (2004). Measurement of detailed heat transfer on a surface under arrays of impinging elliptic jets by a transient liquid crystal technique. *International Journal of Heat and Mass Transfer* 47, 5235–5245.

Yang, H. Q., T. Kim, T. J. Lu and K. Ichimiya (2010). Flow structure, wall pressure and heat transfer characteristics of impinging annular jet with/without steady swirling. *International Journal of Heat and Mass Transfer* 53, 4092–4100.

Yuan, Z. X., Y. Y. Chen, J. G. Jiang and C. F. Ma (2006). Swirling effect of jet impingement on heat transfer from a flat surface to CO_2 stream. *Experimental Thermal and Fluid Science* 31, 55–60.